Research Square

Preprints are preliminary reports that have not undergone peer review.
They should not be considered conclusive, used to inform clinical practice,
or referenced by the media as validated information.

Monotonic increase of conductivity with non-monotonic defect content: ZnO thin films at precursor molar concentrations of 0.3–0.5 M

Andrey Nebesniy

chartamagica@gmail.com

National University of Uzbekistan

Azamat Arslanov

National University of Uzbekistan

Pavel Parchinskiy

National University of Uzbekistan

Abdumanap Nasirov

National University of Uzbekistan

Shavkat Yuldashev

National University of Uzbekistan

Research Article

Keywords: ZnO thin films, ultrasonic spray pyrolysis, hopping charge transport, dielectric relaxation, time–temperature superposition, photoluminescence

Posted Date: September 17th, 2026

DOI: https://doi.org/10.21203/rs.3.rs-10732674/v1

License: This work is licensed under a Creative Commons Attribution 4.0 International License.
Read Full License

Additional Declarations: No competing interests reported.

Monotonic increase of conductivity with non-monotonic defect content: ZnO thin films at precursor molar concentrations of 0.3–0.5 M

A.A. Nebesniy*, A.O. Arslanov, P.B. Parchinskiy, A.A. Nasirov, Sh.U. Yuldashev

Department of Semiconductors and Polymers Physics, National University of Uzbekistan, 4 Universitetskaya str., 100174 Tashkent, Uzbekistan

* Corresponding author. E-mail: chartamagica@gmail.com

ORCID: A.A. Nebesniy 0009-0000-3029-2284; A.O. Arslanov 0009-0000-4817-8770; P.B. Parchinskiy 0009-0008-3812-9383; A.A. Nasirov 0000-0002-7683-5667; Sh.U. Yuldashev 0000-0002-2187-5960

Acknowledgments: This work was supported by the Ministry of Higher Education, Science and Innovation of the Republic of Uzbekistan (Grant No. FZ-2020092435).

Abstract

A diagnostic widely used to identify changes in hopping-conduction mechanism turns out not to work as advertised: the exponent of the Jonscher power law, evaluated within a fixed frequency window, still swings with temperature even when the underlying conductivity spectra do not. For ZnO thin films grown by ultrasonic spray pyrolysis at precursor molar concentrations of 0.3, 0.4 and 0.5 M, the spectra collapse onto a single temperature-independent master curve (scatter 0.004–0.028 decades), yet spectra reconstructed from that unchanged curve still reproduce 45–49 % of the exponent's observed temperature swing – nearly half of what is usually read as a mechanism change is an artefact of where the fixed window happens to sit on the curve. The position of the dielectric relaxation is free of this artefact and gives an activation energy that matches the dc value directly. Applying both measures across the concentration series (with atomic force microscopy, X-ray diffraction, reflectance and temperature-dependent photoluminescence for the optical and structural side) shows charge-transport parameters varying monotonically with concentration while the point-defect content and surface relief are non-monotonic and peak at 0.4 M. Since the band-edge position itself does not differ between samples, the transport differences originate from in-gap states rather than the band structure, and no single concentration is best by every measure. To our knowledge this is also the first impedance-spectroscopy study of undoped ultrasonic-spray-pyrolysis ZnO films over 95–370 K.

Keywords: ZnO thin films; ultrasonic spray pyrolysis; hopping charge transport; dielectric relaxation; time–temperature superposition; photoluminescence.

1. Introduction

Zinc oxide is a wide-band-gap semiconductor ($E_g \approx 3.37$ eV at 300 K) with a large exciton binding energy (~60 meV) [1], used in ultraviolet optoelectronics, transparent conductive coatings and gas sensing. Its functional properties are governed largely by native defects (oxygen vacancies, zinc interstitials and zinc-vacancy complexes), which create localised states in the gap and control both radiative processes and charge transport [1,2].

Ultrasonic spray pyrolysis is attractive for its simplicity, low cost and the control it offers over film composition and thickness through the precursor concentration; films grown this way reach device quality [3]. The influence of molar concentration on the structure and optics of ZnO has been studied repeatedly [4-7]; both a monotonic improvement of film characteristics with increasing concentration and the existence of an optimum have been reported, and the conclusion depends on which characteristic is adopted as the measure of quality. A systematic comparison of concentration with charge-transport mechanisms – particularly under ac excitation, where the frequency dispersion of the conductivity and the dielectric relaxation are directly sensitive to the type of hopping transport [8] – has been made far less often, although it is precisely the joint analysis of transport and optical data that separates physically different kinds of disorder that look alike when taken one at a time. Impedance spectroscopy of sprayed ZnO films has been performed at 610–710 K [9], while low-temperature measurements were made on bulk and nanostructured

material [10,11]; the combination of an undoped ultrasonic-spray-pyrolysis film with impedance spectroscopy over 95–370 K does not appear in the literature.

Here we report a joint analysis of morphology, optical properties and dc and ac charge transport for three ZnO films grown at precursor molar concentrations of 0.3, 0.4 and 0.5 M. The central result is that the picture of a monotonic improvement of quality with concentration is incomplete: charge-transport parameters, optical measures of defect content and surface morphology vary independently of one another in this series, so that no single "film quality" parameter exists for them. The argument is built up in order: from morphology and crystal structure (Section 3.1) through the optical characteristics (Section 3.2) to charge transport (Sections 3.3–3.4), and is brought together in Section 3.5.

2. Experimental

2.1. Film synthesis

ZnO films were deposited by ultrasonic spray pyrolysis onto Si (100) substrates. The substrates were cleaned for 10 min each in hydrofluoric acid (removal of the native oxide), acetone and ethanol (removal of organic contamination), followed by a rinse in deionised water. Zinc acetate dihydrate $Zn(C_2H_3O_2)_2 \cdot 2H_2O$ dissolved in deionised water served as the precursor; solutions with molar concentrations of 0.3, 0.4 and 0.5 M were prepared.

The aerosol was generated by an ultrasonic nebuliser operating at 1.7 MHz and carried into the reaction chamber by an oxygen flow (500 cm^3/min), which also acted as the oxidiser during pyrolysis. The substrate temperature was 450 °C and the deposition time 20 min for all three samples; after deposition the films were annealed in air at 550 °C for 15 min. Film thickness, which for ZnO films is usually obtained from ellipsometry or interference [12], was determined here by two independent routes: from the interference pattern in the specular reflectance spectra with a transfer-matrix calculation (120, 260 and 230 nm for 0.3, 0.4 and 0.5 M), and from the capacitance of the contact–film–substrate structure measured at 300 K above 50 kHz, where the contact pad itself acts as the top electrode ($d = \varepsilon_0 \varepsilon_{ZnO} \cdot A/C$ with $\varepsilon_{ZnO} = 8.5$ and $A = \pi(0.75$ mm$)^2$ gives 125, 320 and 227 nm). The two routes agree to within 4 % for 0.3 and 0.5 M and 23 % for 0.4 M, and back-calculation using the reflectance thicknesses returns $\varepsilon_{ZnO} = 8.2$, 6.9 and 8.6 against the tabulated 8.5; the reflectance thicknesses are used throughout. For an identical deposition time the thickness varies non-monotonically with concentration, i.e. the growth rate does not follow the precursor concentration linearly – a non-monotonic dependence of deposition rate on molarity has been reported previously [7], as has a decrease of thickness at higher concentration [6]. The samples are hereafter labelled by precursor concentration: 0.3 M, 0.4 M and 0.5 M. The same series was studied earlier [4], where its structural and optical characteristics are reported; the present work addresses dc and ac charge transport and its comparison with the optical data.

2.2. Measurement methods

Surface morphology was studied by atomic force microscopy in contact mode: 8 × 8 μm^2 areas, 512 × 512 points (15.6 nm step), with central 384 × 384 point fragments (6 × 6 μm^2) used for quantitative analysis. The relief was levelled by subtracting a second-order surface fitted over the analysed fragment; grains were segmented by a watershed transform driven by surface curvature (Laplacian of Gaussian, $\sigma = 1.2$ points), excluding grains touching the frame border, which yielded 2267–2435 grains per sample. X-ray diffraction was performed on a Shimadzu XRD-6100 diffractometer (Cu Kα, $\lambda = 1.5406$ Å) over $2\theta = 30$–60°, with the bare substrate recorded separately over 20–60°; all diffractograms were obtained on the same instrument under identical conditions, so structural characteristics are extracted from within-series comparison and from intensity ratios. Reflectance spectra were recorded on a Yoke M 601 S-X spectrophotometer over 190–1100 nm. Photoluminescence was excited by a UV laser peaking at 320 nm with 26 mW power at oblique incidence; emission normal to the film was collected onto the slit of an MDR-23 monochromator (1200 grooves/mm, 0.1 mm slits; resolution ≈1.2 meV near the near-band-edge line), detected by a PMT-100

photomultiplier and recovered with an SE1022D DSP lock-in amplifier modulating the excitation at 2 kHz. Spectra were measured at 78–400 K over 350–630 nm under identical excitation conditions. The samples were mounted in a liquid-nitrogen bath cryostat, in which the electrical measurements were also carried out in the dark.

The dc and ac measurements were made in a two-probe configuration on the same contacts – aluminium pads 1.5 mm in diameter, vacuum-evaporated through a shadow mask, with a centre-to-centre spacing $L \approx 7$ mm. The temperature dependence of resistance was recorded with an ITECH IT2805 source-measure unit over 96–370 K; the measured resistance was converted to sheet resistance through the planar thin-layer expression $R = (R_s/\pi)\cdot\ln(L/a)$, where a is the contact radius, which requires no knowledge of the film thickness. Because the measurement is two-probe, R_s contains the contact resistance and the quoted values are upper bounds. For the 0.4 M sample a correction was applied for a parallel shunting channel, which manifests itself as a plateau of R(T) at low temperatures; its magnitude, $9.3 \times 10^5 \pm 0.4 \times 10^5$ Ω, was obtained by fitting the low-temperature branch. The correction is significant below 200 K and does not exceed 10 % above 300 K; it is applied to every quantity quoted for 0.4 M and is essential: without it the T_0 parameter of this sample would be 7.0×10^3 instead of 7.2×10^4 K. The nature of the channel is not established: within the fitting interval it is temperature-independent, which is uncharacteristic of conduction through the substrate, and it is observed only for 0.4 M; the associated uncertainty is propagated into the error bars quoted below. Impedance spectroscopy was carried out on a Rohde & Schwarz HAMEG HM8118 LCR bridge over 20 Hz–200 kHz at 95–370 K with a 100 mV test-signal amplitude.

Every impedance spectrum was tested against the criterion $\sigma'(\omega) \geq \sigma_{dc}$: the real part of the conductivity cannot fall below its static limit, measured independently in dc on the same contacts. For 0.5 M the ratio $\sigma'(20\ \text{Hz})/\sigma_{dc}$ is constant at 0.67 ± 0.06 over the whole 96–370 K range, i.e. it corresponds to a systematic offset between the two measurements and does not affect the slopes of the temperature dependences. For 0.4 M the criterion is violated at every temperature, so absolute values of its ac conductivity are not quoted and only the spectral shape is used. For 0.3 M the ratio falls from 1.34 at 200 K to 0.27 at 355 K and is described by adding a series element of 84–116 kΩ to the impedance model, whose influence grows with frequency; this element cannot be an ohmic series resistance in the dc circuit, since it exceeds the total measured resistance of the sample at high temperatures (Section 3.3), and its nature remains unidentified. Accordingly, the 0.3 M data are used up to 310 K at frequencies not exceeding 1 kHz and up to 275 K at higher frequencies, while spectra at 324 K and above are excluded entirely.

Since the films are grown on silicon, the substrate contribution was checked separately. The substrates are n-type silicon; the wafer resistivity measured at 300 K is about 555 Ω·cm, corresponding to a donor concentration of $\approx 9 \times 10^{12}$ cm^{-3}, and the measured capacitance of the contact–film–substrate structure (1066, 416 and 586 pF) agrees with $\varepsilon_0\varepsilon_{ZnO}\cdot A/d$ to within 20 % with no fitting parameters. This confirms the vertical character of the high-frequency capacitance (in pad-on-film-on-silicon structures the measured capacitance is determined by the structure as a whole [13]), justifies the thickness estimate of Section 2.1, and implies the absence of series capacitances in this path. A depletion layer in the silicon at this doping level would be 7–11 μm wide and would contribute a series capacitance of 17–28 pF, i.e. the measured value would be one and a half orders of magnitude smaller than observed; the thickness of any interfacial SiO_2 layer is bounded above by ≈2 nm, that is, it does not exceed a native oxide. Both facts matter for the parasitic-branch estimate below: its capacitance is limited neither by depletion nor by an interfacial dielectric, so the estimate given is conservative. The dc measurement itself bounds the resistance of any parallel path through the substrate from below by the measured sample resistance (2.2×10^5, 8.8×10^4 and 2.8×10^4 Ω), since otherwise the film resistance obtained from the parallel-combination expression would be negative. In addition, silicon of this resistivity freezes out on cooling, whereas the shape of the conductivity spectra is unchanged over the whole 96–370 K range (Section 3.4).

This suffices for dc, but capacitive coupling operates only under ac excitation, so the parasitic path contact–film–substrate–film–contact was evaluated quantitatively. It consists of two vertical capacitances in series

with the spreading resistance in the silicon; both quantities were measured independently – the capacitances are given above, and the lateral wafer resistance between two 1.5 mm diameter contacts is 11.7 kΩ at a spacing of 5.5 mm, which scales to 12.5 kΩ at the working spacing of 7 mm. The branch impedance is $Z_{par} = R_{sp} + 2/(j\omega C)$, where C is the measured structure capacitance and R_{sp} the spreading resistance in the substrate; the crossover frequency follows from $|Z_{par}| = R_{film}$, i.e. $2/(\omega C) = (R_{film}^2 - R_{sp}^2)^{1/2}$, where R_{film} is the lateral film resistance at 300 K (2.2×10^5, 8.8×10^4 and 2.8×10^4 Ω). The two-probe value R_{sp} = 12.5 kΩ contains the contact resistance and is therefore an upper bound, and overestimating R_{sp} overestimates the crossover frequency as well; the conservative choice $R_{sp} = 0$ is therefore adopted, giving 1.4, 8.7 and 19 kHz for 0.3, 0.4 and 0.5 M. The entire ac analysis is restricted to frequencies below these values. The time constant of the parasitic branch is set by a geometric capacitance and by the silicon resistance, which does not freeze out above ≈150 K, and is therefore essentially temperature-independent (the corresponding frequencies are 24, 61 and 43 kHz at R_{sp} = 12.5 kΩ), whereas the observed characteristic response frequencies shift with temperature by factors of tens to hundreds (Section 3.4).

2.3. Processing of the photoluminescence spectra

Spectra were converted to an energy scale with the λ^2/hc Jacobian, without which band positions and widths are systematically distorted, and were calibrated against the second-order diffraction of the excitation line (640 nm). All three samples were measured in one session on the same optical train, so the spectral sensitivity of the system is common to them. The gain of the detection chain differed between samples, so absolute intensities are not comparable and all comparisons are made through band ratios within a single spectrum, on which the gain has no effect. No spectral-response correction against a reference lamp was applied; the factor entering I_{def}/I_{NBE} that accounts for the change of sensitivity between 375 and 502 nm is the same for all three samples and cancels when they are compared, so that only a scale factor common to the series remains undetermined while the relative series is exact. Band intensities were obtained by integration above a local linear background defined by reference windows on both sides of the band. The parameters α and β of the Varshni model [14] are degenerate over the accessible interval, so β was fixed at 900 K and the LO-phonon energy in the broadening model at 72 meV [1]. Decomposition of the near-band-edge line into Gaussian components was performed by variable projection, the number of components being selected by an information criterion together with physical constraints.

3. Results and discussion

We begin with the surface morphology and crystal structure of the films: they set the frame of reference in which the optical and transport data are examined below.

3.1. Morphology, structure and grain size

The surface of all three films consists of close-packed grains with mean equivalent diameters of 130 ± 30, 129 ± 31 and 134 ± 33 nm for 0.3, 0.4 and 0.5 M. The difference between samples (≈4 nm) is much smaller than the systematic spread of the estimate under variation of the smoothing parameters (±12 nm), as is the difference between distribution widths: neither the grain size nor its spread distinguishes the samples. Allowing for broadening introduced by the finite tip radius, 130 nm should be regarded as an upper bound.

The differences appear in the large-scale relief. The 0.4 M sample carries, on a uniform granular matrix, sparse agglomerates 400–450 nm across (individual ones up to 800 nm) rising some 20 nm above the surrounding surface – twice as high as features of the same scale in the other two samples (Fig. 1b). Accordingly, it shows the largest root-mean-square roughness (S_q = 16.9 nm against 13.4 and 13.1 nm), height-distribution skewness (S_{sk} = 0.76 against 0.13 and 0.03) and relief correlation length (L_c = 123 nm against 68 and 73 nm), while 0.3 and 0.5 M are virtually indistinguishable by these measures. The morphological inhomogeneity is therefore non-monotonic in concentration and maximal at 0.4 M.

Since only one scan is available per sample, the robustness of these differences was checked by dividing the analysed fragment into nine independently levelled 2×2 μm^2 sub-regions. The median roughness over them

is 13.0, 17.0 and 12.5 nm, reproducing the whole-fragment values, and the excess for 0.4 M persists in eight sub-regions out of nine. The scatter between sub-regions itself distinguishes the samples (0.7 and 0.9 nm for 0.3 and 0.5 M against 2.2 nm for 0.4 M), as expected for sparse agglomerates that do not fall into every sub-region. This test is confined to a single field of view and does not replace imaging of several areas.

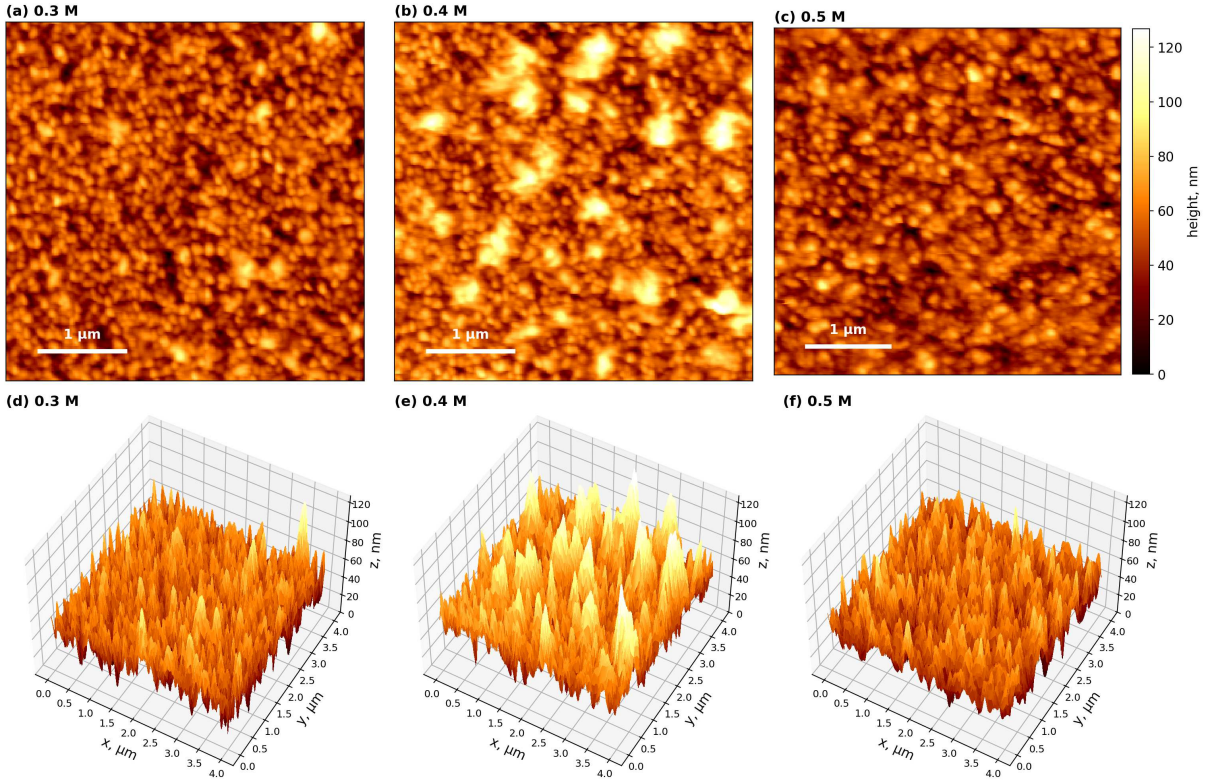


Fig. 1 AFM images of the ZnO film surfaces for 0.3, 0.4 and 0.5 M: (a–c) relief maps of the central $4 \times 4\ \mu m^2$ parts of the analysed fragments, on a common height scale, (d–f) the same areas in three-dimensional representation. Large agglomerates, absent in the other two samples, are clearly visible for 0.4 M

X-ray diffraction was used for independent structural characterisation, with the bare substrate recorded separately under identical conditions (Fig. 2). The films are phase-pure: all reliable reflections belong to hexagonal wurtzite ZnO – the dominant (002) at $2\theta \approx 34.3$–$34.4°$, and weak (100) at 31.8° and (101) at 36.25°. The remaining peaks, including the intense narrow reflection at 43.8°, are also present in the scan of the bare substrate and therefore do not belong to the film; no secondary phases were found in the films. Two of them lie close to wurtzite reflections, 47.85° to (102) at 47.54° and 56.4° to (110) at 56.60°, so these two ZnO reflections are excluded from the analysis. As a set, the lines (37.6, 43.8, 46.2, 47.85, 54.65, 55.5 and 56.4°) index neither as silicon reflections nor as any phase of ZnO, and their intensity varies between mountings by factors of 3–38 while their positions stay fixed, which is characteristic of multiple diffraction in a single-crystal wafer. They cannot therefore be used as an intensity standard, and no quantitative comparison of the crystallinity of the samples is made from the diffraction data.

All three films are strongly c-axis textured, which is the norm for sprayed ZnO films [15]. For a randomly oriented powder the strongest ZnO reflection is (101), whose tabulated intensity exceeds that of (002) by more than a factor of two; the opposite is observed in our scans. Since the (101) line does not rise above the background, the (002)/(101) ratio is a lower bound: $I(002)/I(101) \gtrsim 5$, 3 and 2 against an expected 0.44. The substrate scan shows no lines in the 34.3–34.4° region, so the (002) intensity belongs entirely to the film. The texture cannot be quantified: the (100) line does not rise above the background in any sample and (101) is detected at 0.8–1.7 standard deviations of the background, so texture coefficients, which require all three intensities, are not determined by these data. As with grain size, the samples do not differ in texture.

The effective size of coherently scattering domains from the Scherrer formula (K = 0.9) [16] applied to the width of the (002) reflection is D ≈ 24.5, 29.7 and 28.6 nm. No instrumental correction was applied, so these are lower bounds; given the uncertainty of the peak width (±3–4 nm), the difference between samples lies within the error of the method – in contrast to the systematic growth of this size with concentration reported for sprayed ZnO films [5]. The coherent-domain size is 4–5 times smaller than the grain size seen by AFM (≈130 nm): across its diameter one grain contains about five coherently scattering domains, i.e. of order twenty in cross-section. The grains visible at the surface are therefore agglomerates of nanocrystallites rather than single-crystal domains, which explains why grain size and coherent-domain size behave independently.

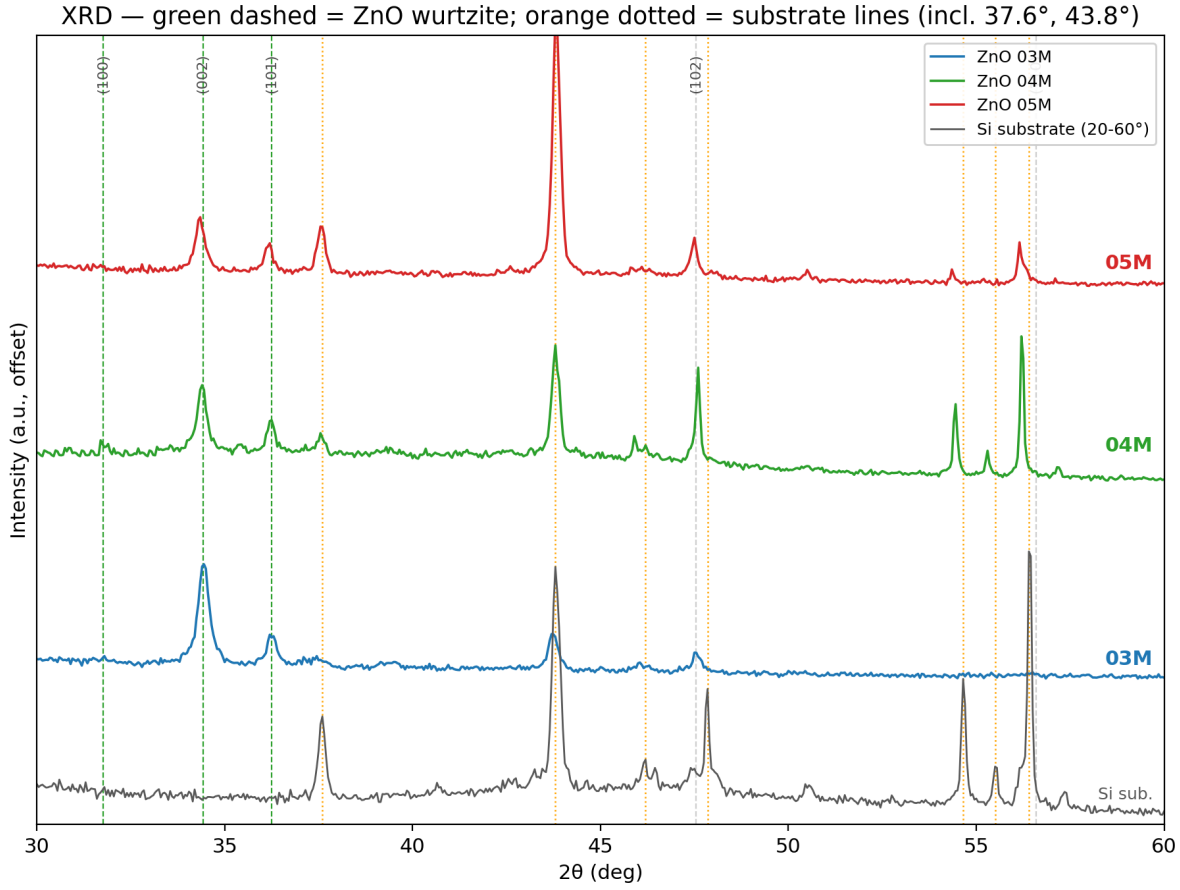


Fig. 2 X-ray diffractograms of the ZnO films and a scan of the bare substrate (bottom curve); curves are offset vertically. Green dashed lines mark the wurtzite reflections (100), (002) and (101); orange dotted lines mark positions of lines also seen in the substrate scan, including the intense reflection at 43.8°. These lines do not belong to the film, but neither do they index as silicon reflections, and their intensity varies strongly between mountings

Morphology and structure on their own say nothing about the point-defect density or the uniformity of the emitting centres. Photoluminescence addresses these questions directly.

3.2. Optical properties

Emission spectra: near-band-edge and defect luminescence

The photoluminescence spectra (Fig. 3) contain a near-band-edge (NBE) line at 3.27–3.35 eV and a broad "green" defect band centred at 2.47 eV (502 nm), most probably associated with vacancy centres [17,18]; the specific assignment remains debated – besides oxygen vacancies, zinc vacancies, complexes with interstitial zinc and a copper impurity are all considered [1,2]. The relative intensity of the defect emission at 300 K differs radically (3.15, 0.037 and 0.49 for 0.3, 0.4 and 0.5 M), and the defect series is non-monotonic: the minimum falls not at the highest concentration but at 0.4 M. For this sample the defect band does not exceed the threshold of reliable detection at any temperature, so the quoted value is an upper bound.

The width of the defect band also differs: 0.357 eV for 0.3 M against 0.179 eV for 0.5 M, i.e. the most defective sample also shows a broader distribution of local environments of the defect centres. For 0.5 M the defect-to-NBE ratio rises sharply above 300 K (from 0.49 to 1.9 at 400 K), because the near-band-edge emission quenches while the defect emission does not.

The ratio I_{def}/I_{NBE} depends on what fraction of the film is excited: at 320 nm the absorption depth in ZnO is 50–67 nm, whereas the thicknesses are 120, 260 and 230 nm. The mean excitation depth is similar for all three samples (39–61 nm) but corresponds to different fractions of the thickness – 0.32–0.36 for 0.3 M against 0.19–0.26 for the other two. This does not affect the main conclusion: samples 0.4 and 0.5 M have essentially the same excitation geometry (relative depths 0.21 and 0.24) yet their I_{def}/I_{NBE} ratios differ by a factor of 13, so the non-monotonicity of the series cannot be explained by an inhomogeneous depth distribution of defects. For 0.3 M, probed relatively more deeply, such a contribution is possible in principle, but the difference in probed thickness fraction is only a factor of 1.5 against a sixfold difference in defect emission relative to 0.5 M.

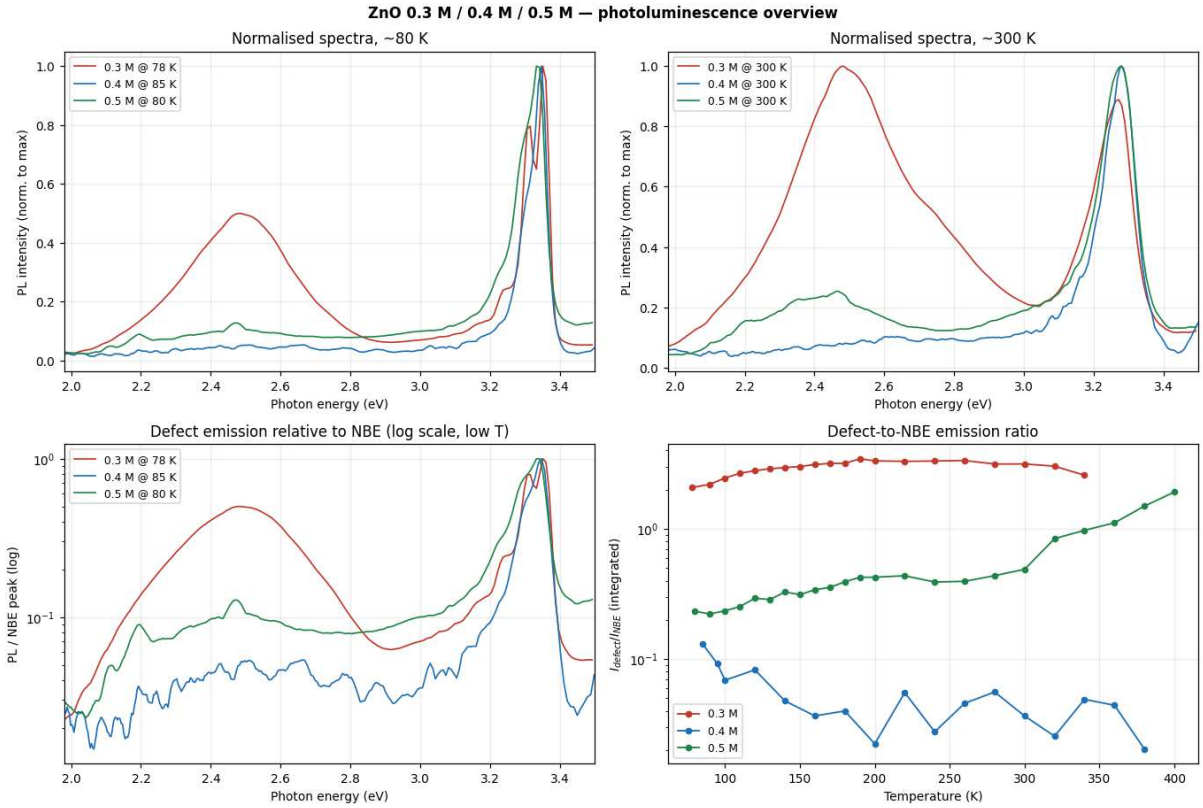


Fig. 3 Overview of the photoluminescence: normalised spectra at ~80 and 300 K, defect emission relative to the near-band-edge line on a logarithmic scale, and the temperature dependence of the integrated I_{def}/I_{NBE} ratio. For comparability all spectra were brought to a common 1 nm grid and smoothed with the same window (1.5 nm near the NBE line, 15 nm in the defect region); smoothing was applied to the display only, and the residual oscillations of the 0.4 M curve correspond to the noise level

Band-edge energy and line broadening

The position of the near-band-edge line shifts to the red with increasing temperature, following the thermal renormalisation of the band gap (Fig. 4). The fit was performed not on the position of the composite line but on the centre of its high-energy Gaussian component: at low temperatures the near-band-edge line resolves into components separated by 21–43 meV, and the redistribution of their weights with temperature feeds directly into the apparent shift of the composite contour. A Varshni fit with β fixed at 900 K gives E_0 = 3.363, 3.358 and 3.357 eV and α = 0.89, 0.99 and 1.11 meV/K. The parameters α and β are degenerate over this interval and β is fixed, so the α series carries no independent meaning and is quoted only as a fit parameter. The uncertainty quoted for E_0 is set not by the fit statistics but by the choice of procedure:

scanning the alternatives (β between 600 and 1200 K, different temperature intervals) gives spreads of ±1, ±6 and ±9 meV for 0.3, 0.4 and 0.5 M, whereas the formal fitting error is three times smaller. For comparison, fitting the position of the composite line gives a spread of E_0 between samples of 22 meV and an anomalously large α = 1.216 meV/K for 0.3 M – the sample in which the doublet is resolved most clearly; both effects are artefacts of the composite contour. An independent Bose–Einstein fit [19] agrees with this one to within 9–14 meV.

The E_0 values differ between samples by 6 meV, i.e. they lie within the stated uncertainty: the band-edge position is the same for the whole series to within the accuracy of the method, in agreement with the independent result from the reflectance spectra (see below). We note that the lattice parameter c determined from the position of the (002) reflection increases monotonically through the series (5.204, 5.210 and 5.218 Å), corresponding to a c-axis strain of about 0.3 %, which at a typical deformation potential would produce a band-edge shift of a few meV – the same order as the observed spread. The absolute reflection positions, however, carry a systematic error from specimen height displacement: a 50–100 μm offset gives $\Delta 2\theta \approx 0.03–0.06°$, i.e. $\Delta d/d \approx 0.1–0.2$ %, comparable with the entire observed spread of 0.27 %. The monotonicity of c is therefore not established by these data, and the estimate indicates only the order of the possible contribution.

The measure of inhomogeneous broadening is the width of the near-band-edge line at low temperature, where the phonon contribution is minimal. The full width at half maximum, taken from the half-height crossing points after subtraction of a local linear background, is 77.6, 63.2 and 84.9 meV. The series is non-monotonic: the smallest broadening is found for 0.4 M and the largest for 0.5 M. The quantity reflects the spread of local environments of the emitting centres and internal strain, and is unrelated to grain size, which by AFM is the same throughout the series. A fit of the full dependence $\Gamma(T) = \Gamma_0 + \gamma \cdot T + \Gamma_{LO}/[\exp(E_{LO}/kT) - 1]$ with E_{LO} = 72 meV gives the same ordering of samples (Γ_0 = 67.7, 56.9 and 75.4 meV).

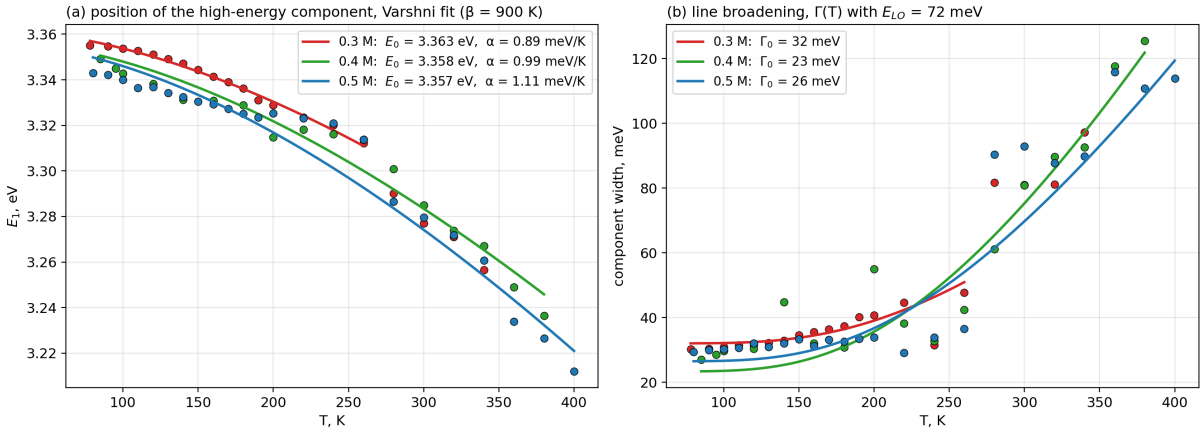


Fig. 4 Temperature dependences of the position and width of the high-energy component of the near-band-edge line: (a) Varshni fit with β fixed at 900 K, (b) phonon broadening model with E_{LO} = 72 meV

Absorption edge

The optical characteristics were analysed from the reflectance spectra. In the region of the absorption edge (Fig. 5) all three samples show a sharp drop of reflectance near 380 nm, with the edge position identical to within the accuracy of the method; the differences in spectral shape at longer wavelengths are due to interference in the thin layer.

The absolute band-gap value cannot be extracted from these spectra. Tauc extrapolation [20] in its various forms – via the Kubelka–Munk function, via absorption reconstructed in the double-pass approximation, and via spectral derivatives – gives 3.18–3.29 eV, and the disagreement between procedures (up to 90 meV) is twice the difference between samples; moreover, most of these values lie below the position of the photoluminescence line at 300 K (3.269, 3.277 and 3.276 eV), which is impossible for excitonic emission. The reason is that what is measured is relative specular reflectance of a film on an opaque substrate: the

signal is modulated by interference and bounded from below by the stray-light level. The absorption edge is therefore characterised only qualitatively – near 3.2–3.3 eV, the same for all three samples – while the quantitative measure of the band edge is E_0 from the temperature dependence of the photoluminescence line.

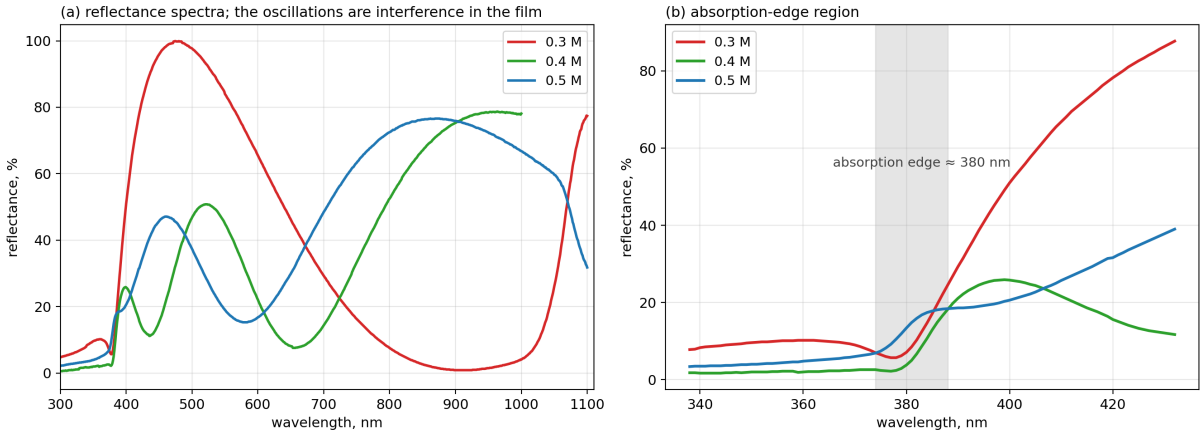


Fig. 5 Specular reflectance spectra of the ZnO films: (a) full measured range, where the oscillations correspond to interference in the film and differ because of the different thicknesses; (b) the absorption-edge region – in all three samples the edge lies near 380 nm

The near-band-edge linewidth discussed above characterises the static inhomogeneity of the emitting states at a fixed temperature. Additional information – on deep non-radiative centres and on the fine structure of the line itself – comes from the thermal quenching of the emission.

Thermal quenching and fine structure of the near-band-edge line

Quenching of the near-band-edge line was described by a two-channel Mott–Seitz model [21] $I(T) = I_0/[1 + \Sigma C_i \exp(-E_i/kT)]$ (Fig. 6). The total quenching depth over each sample's own interval is 1.7, 4.8 and 8.0 times, and when reduced to a common interval up to 340 K it becomes ≈2.6, 4.2 and 4.5, the value for 0.3 M being the larger of the two because its quenching is non-monotonic (see below): 0.4 and 0.5 M almost coincide, and only the weakened quenching of the most defective 0.3 M stands out reliably. The extended interval up to 380–400 K, available for 0.4 and 0.5 M, reveals a dominant high-temperature channel with energies $E_2 = 264 \pm 49$ and 334 ± 30 meV, i.e. the channel corresponds to a deep non-radiative centre with a depth of order 260–360 meV. This range does not follow the widely differing activation energies of the conductivity (233, 164 and 95 meV) and diverges from them most sharply for 0.5 M: luminescence quenching and high-temperature charge transport are controlled by different states.

For the 0.3 M sample the quenching is anomalously weak and non-monotonic: the intensity falls up to ~140 K, then reaches a plateau and partly recovers, so quenching energies are not quoted for it. This is a reproducible feature of the most defective sample – "negative thermal quenching" [21-23], in which carriers released from shallow traps over an intermediate temperature range partly feed the near-band-edge radiative channel.

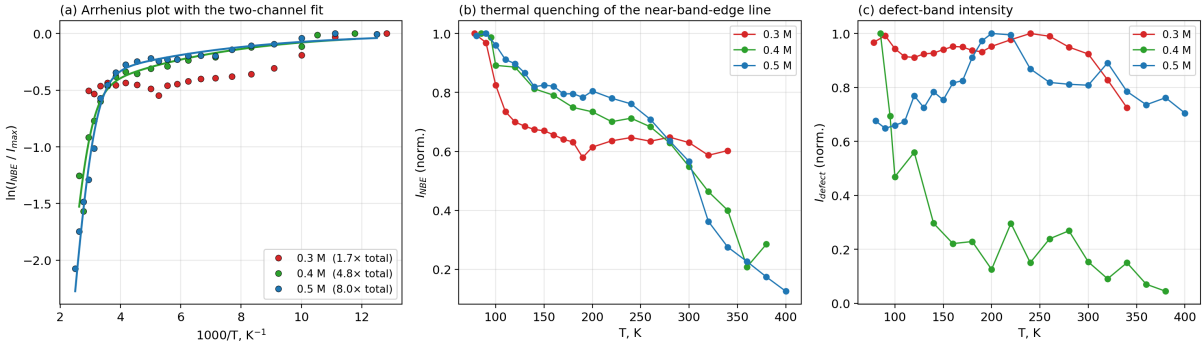


Fig. 6 Thermal quenching of the near-band-edge emission in Arrhenius coordinates with a two-channel Mott–Seitz fit. For 0.3 M the quenching is non-monotonic and the energy is not determined

Decomposition of the near-band-edge line into Gaussian components (Fig. 7) robustly reveals at least two components at low temperatures in every sample. The splitting between the two high-energy components, ΔE_{12}, is essentially temperature-independent and distinguishes the samples reliably: 42.6 ± 0.9, 21.5 ± 2.6 and 26.8 ± 0.8 meV. For 0.3 M the doublet is resolved explicitly: at 78 K it appears in the measured spectrum as two separate maxima (3.355 and 3.312 eV).

The ΔE_{12} series is non-monotonic and repeats the defect series, which points to a defect-related origin of the low-energy component of the doublet. A third component lies 65–93 meV away, corresponding to 0.90–1.29 of the ZnO LO-phonon energy (72 meV) and consistent with its interpretation as a phonon replica. As the temperature rises the number of distinguishable components decreases, and by 340–400 K only a single broad line remains.

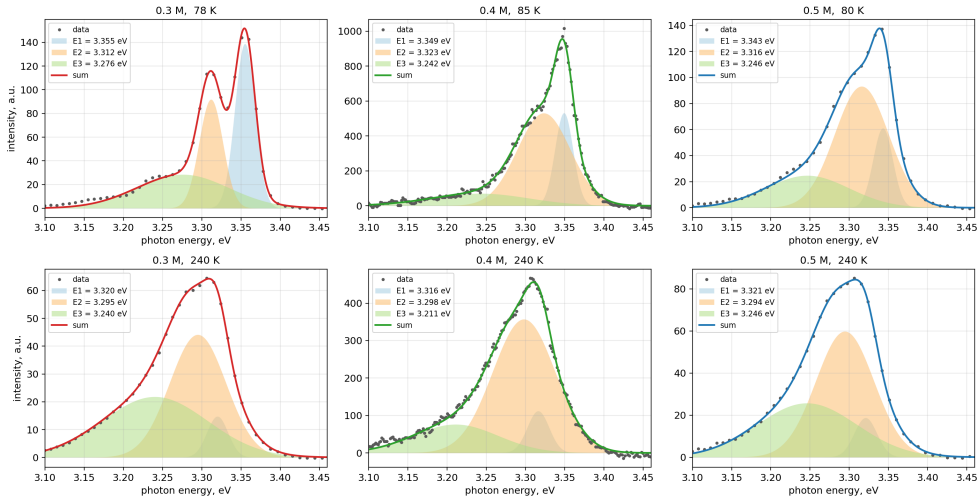


Fig. 7 Decomposition of the near-band-edge line into Gaussian components at low temperature; components are numbered by energy

The optical measurements of Section 3.2 show that the point-defect content and the uniformity of the emitting states vary non-monotonically with precursor concentration. Whether this correlates with charge transport is shown by the temperature dependences of the dc resistance.

3.3. Direct-current charge transport

The temperature dependences of the resistance (Fig. 8a) are clearly non-Arrhenius in the low-temperature range: simple activation would require the activation energy to grow from 17 to 60 meV over 96–200 K. They are linearised satisfactorily in ln R versus $T^{-1/4}$ coordinates, corresponding to three-dimensional Mott variable-range hopping [24-26], over a common interval 96–200 K (Fig. 8b). The exponent itself, however, is not determined by these data. Zabrodskii analysis [27] (the slope of ln w versus ln T, where $w = -d(\ln R)/d(\ln T)$, which yields the exponent directly) gives no linear dependence (R^2 = 0.28–0.55), and the extracted values range from 0.1 to 1.5 between samples. Comparing the goodness of fit of pre-selected forms does not settle the question either: the coefficients of determination for exponents 1/4, 1/3, 1/2 and 1 differ in the fourth decimal place, and for 0.4 M the 1/3 and 1/2 models describe the data no worse than Mott's, while the Efros–Shklovskii model [28] is virtually indistinguishable from it. The reason is the narrowness of the accessible interval: $T^{-1/4}$ changes by only 20 % across it while ln R changes by 0.8–1.3. The $T^{-1/4}$ dependence is therefore used below as an empirical description, not as an established transport mechanism. Deviation from Mott linearity sets in at 191, 173 and 162 K: the higher the precursor concentration, the earlier the crossover to the activated regime. The crossover is extended rather than sharp: the local activation energy continues to rise for another 120–150 K above these temperatures (Fig. 8c), so the values quoted

mark its onset rather than a transition point. The high-temperature Arrhenius branches were analysed over a common interval of 310–355 K.

All the key transport parameters vary monotonically with concentration. The parameter T_0, which characterises the steepness of ln R versus $T^{-1/4}$, falls by more than an order of magnitude: 4.3×10^5, $(7.2 \pm 1.0) \times 10^4$ and 3.3×10^4 K, where the uncertainty for 0.4 M reflects the uncertainty of the parallel-channel correction (Section 2.2); the deviation temperature is insensitive to it. The high-temperature activation energy decreases from 233 to 164 and 95 meV – appreciably below the values typical of double Schottky barriers at the grain boundaries of sintered varistor ceramics [29], which is natural for an unsintered film, and close to values reported for doped ZnO films [30]. The sheet resistance at 300 K decreases from 3.1×10^5 to 1.2×10^5 and 4.0×10^4 Ω/sq – the conductance rises by factors of 2.5 and 7.8 relative to 0.3 M; this quantity is measured directly and requires no knowledge of the thickness. With the thicknesses of Section 2.1 it corresponds to conductivities of 0.27, 0.31 and 1.09 S/cm at 300 K. The capacitance-derived thicknesses give 0.26, 0.25 and 1.10 S/cm, i.e. for 0.3 and 0.4 M the two thickness estimates bracket the same value and the conductivities of these two samples are not separated; the monotonic quantity is the sheet resistance, which requires no thickness at all.

The two-probe geometry does not allow the contact resistance to be separated, but its contribution is bounded from above and cannot generate the observed series. First, a temperature-independent series resistance always lowers the apparent activation energy, so it can only weaken, not create, a monotonic trend in which the largest energy belongs to the most resistive sample; subtracting a series resistance shifts E_a and T_0 upwards. Second, the measurement itself provides a direct bound: the total resistance of the 0.3 M sample is 6.2×10^4 Ω at 355 K and 4.7×10^4 Ω at 369 K, so an ohmic series element of that magnitude or larger is excluded. Subtracting 10 kΩ changes T_0 by 2 %, and subtracting 47 kΩ – a deliberately excessive estimate equal to the entire sample resistance at the upper measurement limit – changes it by 11 %. Third, the position of the dielectric relaxation maximum does not depend on the series resistance at all, and the energies obtained from it (159 ± 6 meV for 0.4 M and 106 ± 5 meV for 0.5 M) agree with the dc values (164 and 95 meV) to within 3 and 12 %, which shows the absence of a dominant contact contribution for these samples. For 0.3 M this check is impossible because its high-temperature impedance data were rejected: for the sample that defines the upper ends of both monotonic series there is no independent confirmation, and the contact contribution is bounded only by the first two arguments.

If the Mott interpretation is nevertheless adopted, the localisation length ξ and the density of states $N(E_F)$ can formally be estimated from T_0 and the prefactor, but the conditions of validity of the model are met only marginally: $R_{hop}/\xi \approx 1.2$–3.1 and $W/k_BT \approx 0.8$–2.0 instead of the required $R_{hop} \gg \xi$ and $W \gg k_BT$, and for 0.3 M the formal estimate of ξ comes out smaller than the interatomic spacing. ξ and $N(E_F)$ are therefore not quoted, and T_0 is used as an empirical measure of the steepness of ln R versus $T^{-1/4}$. The very fact that the estimate fails for 0.3 M points independently to it as the most strongly localised sample, in agreement with its maximal T_0.

The local activation energy $E_a(T) = d(\ln R)/d(1/T)$ (Fig. 8c) rises from 20–50 meV in the hopping regime, passes through a maximum inside the measured interval (246, 176 and 106 meV at 342, 325 and 277 K for 0.3, 0.4 and 0.5 M) and then falls. For 0.3 and 0.4 M the values quoted above, obtained by fitting in the common 310–355 K window, lie close to these maxima and are not lower bounds; for 0.5 M, whose maximum falls at 277 K, the window lies beyond it, on the descending branch. The decrease of $E_a(T)$ at high temperatures is expected when a parallel conduction channel that grows with temperature switches in; for the 0.4 M sample such a channel is identified explicitly and accounted for (Section 2.2). In the fixed 310–355 K window the quoted values correspond to different parts of the curve – for 0.5 M this is already the descending branch – so they should be compared as a ranking of samples rather than as energies of one and the same process. The monotonicity of the series does not depend on the choice of window: the maxima of $E_a(T)$ themselves, 246, 176 and 106 meV, reproduce the same ordering as the values 233, 164 and 95 meV obtained in the fixed window.

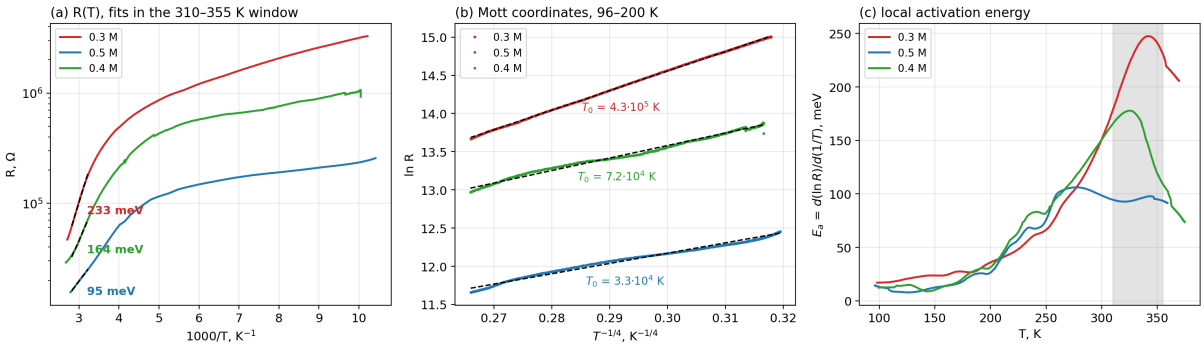


Fig. 8 Direct-current charge transport: (a) R(T) in Arrhenius coordinates with fits in the common 310–355 K window; (b) linearisation in ln R versus $T^{-1/4}$ coordinates over 96–200 K; (c) local activation energy $E_a = d(\ln R)/d(1/T)$, with the 310–355 K window shaded. The 0.4 M data are shown with the parallel-channel correction applied (Section 2.2)

Direct current gives an integral characteristic of charge transport. A more detailed picture of carrier localisation and of the relaxation processes is provided by the alternating-current response.

3.4. Alternating-current conductivity and dielectric relaxation

The frequency dependences of the real part of the conductivity of all three samples have the shape usual for disordered systems: a low-frequency plateau corresponding to the static conductivity, and a power-law rise above a characteristic frequency (Fig. 9a). The samples differ in the magnitude of this rise: at 250 K the ratio of σ′ at the upper end of the range to its value at 20 Hz is 64, 102 and 6.9. The values quoted in this paragraph are computed over the whole measured range up to 200 kHz and are descriptive; they are not used in the quantitative conclusions, which rely only on the region below the crossover (Section 2.2). The impedance phase at 20 Hz singles out the same sample: −29.7°, −9.7° and −0.8°, i.e. the low-frequency response of 0.5 M is almost purely resistive, whereas in the other two a noticeable fraction of the current is capacitive. The two measures rank 0.3 and 0.4 M differently because they weight different parts of the spectrum, the dispersion ratio the high-frequency end and the phase at 20 Hz the low-frequency one.

In complex-impedance coordinates (Fig. 9b) the response does not reduce to a single relaxation process: for 0.3 M at 250 K two arcs are distinguishable, while for 0.4 and 0.5 M they overlap into one markedly depressed arc. Separation of the response into grain and grain-boundary contributions via two arcs of the Nyquist plot is documented for ZnO [31]. The spectra are well described by two parallel R–CPE elements (a resistor in parallel with a constant-phase element) connected in series. The presence of two processes is confirmed without any fitting: for a single RC element the maxima of Z″(f) and M″(f) must coincide, whereas the measured ratio of their frequencies is 4.1, 4.6 and 55; the ZnO literature usually stops at stating the non-Debye character of the relaxation [10], whereas here the separation of the peaks is used quantitatively. The constant-phase exponent of the slow element is 0.82, 0.85 and 0.78, and the width of the Z″ peak at half height is 1.77 and 1.69 decades for 0.4 and 0.5 M against 1.144 decades for a Debye process. The distribution of relaxation times is thus about one and a half times broader than Debye, but the samples are not distinguished by this feature.

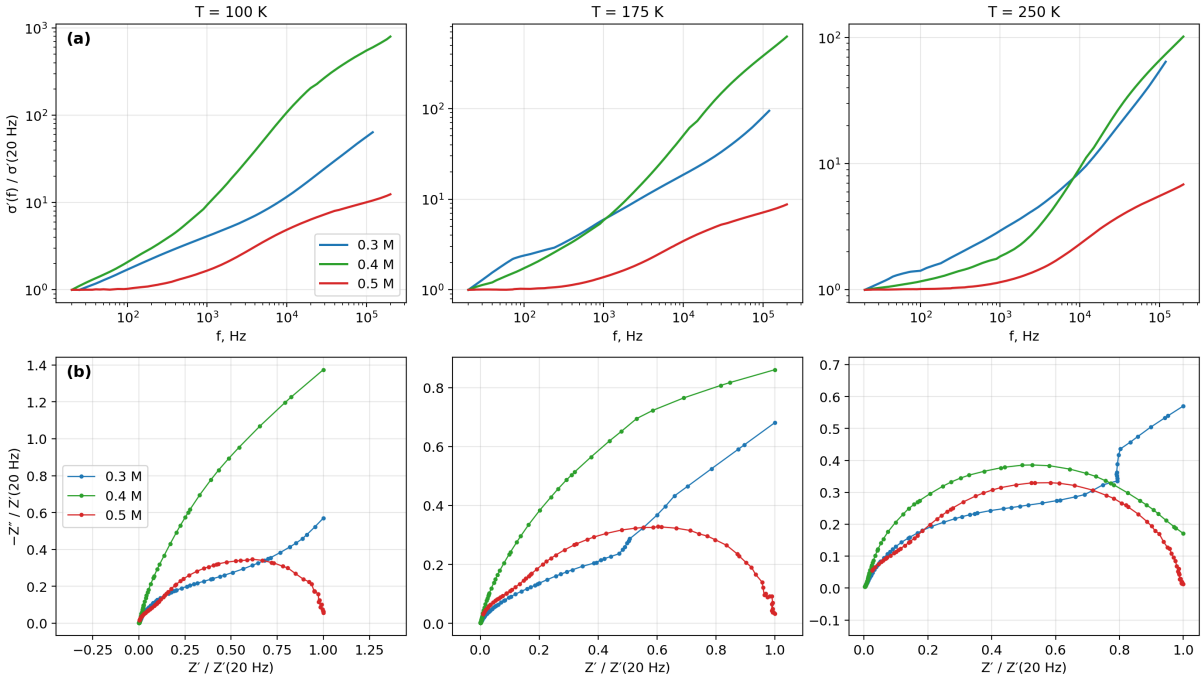


Fig. 9 Alternating-current response at three common temperatures: (a) conductivity dispersion normalised to the value at 20 Hz; (b) impedance Nyquist plots normalised to Z′(20 Hz). Measured quantities only, with no fitting parameters

To establish whether the transport mechanism changes with temperature, the spectra were reduced to the dimensionless form σ'/σ_{dc} versus f/f_H, where the characteristic frequency f_H is defined from the data themselves by the condition $\sigma'(f_H) = 2\sigma_{dc}$ and is not a fitting parameter [32-34] (Fig. 10). Within the frequency window used, the curves collapse onto a single master curve with median scatters of 0.012, 0.004 and 0.028 decades – over 15, 38 and 30 temperatures in the intervals 97–275, 96–340 and 96–288 K. When the frequency restriction is lifted, i.e. when the region dominated by the parasitic branch (Section 2.2) is included, the collapse does not improve but degrades – to 0.073 and 0.043 decades for 0.3 and 0.4 M. If the collapse were produced by a fixed parasitic RC element, excluding precisely the region where it operates should have destroyed it; the opposite is observed. The same result is reproduced in the impedance representation: the normalised curves Z''/Z''_{max} versus f/f_{max} converge with scatters of 0.037 and 0.032 decades for 0.4 and 0.5 M.

The median scatter over all points, however, underestimates the true disagreement by construction: both axes are normalised to σ_{dc}, and f_H is defined by the condition $\sigma'(f_H) = 2\sigma_{dc}$, so all curves are forced through a common point whose neighbourhood artificially improves the estimate. The scatter was therefore computed separately over decades of $\log_{10}(f/f_H)$. For 0.3 M it is not minimal near that point (0.017 in the decade above f_H against 0.007 below it), so the anchor does not influence the overall estimate. For 0.5 M, by contrast, the scatter is 0.002 near the anchor and rises to 0.043 on the low-frequency wing, and for 0.4 M it likewise falls to 0.001 near the anchor against 0.006 below it, so for these two samples the overall figure is an optimistic bound. A check with an independent scaling in which the frequency axis is built from the dielectric strength rather than from the static conductivity [33] gives scatters of 0.14, 0.13 and 0.07 decades. Strict time–temperature superposition therefore holds for none of the samples, and what is observed is an approximate collapse of the spectral shape.

The deviation of the 0.5 M sample is systematic rather than random: the departure from the master curve is monotonically related to temperature (the Spearman rank correlation coefficient, computed over the frequency-median residuals at each temperature so as not to inflate the significance through dependent points within one spectrum, is -0.95 with $p \approx 2 \times 10^{-15}$ and $n = 30$; low temperatures lie above high ones), and on the low-frequency wing its amplitude reaches 0.043 decades. For 0.3 M no such relation is found (-0.49 with $p = 0.07$ and $n = 15$). For 0.4 M the correlation is formally significant but has the opposite sign

and an amplitude seven times smaller (+0.56 with $p = 3 \times 10^{-4}$ and n = 38; residual 0.006 decades), so it does not indicate a change of the same kind. At the same time 0.5 M is the only sample for which the break in the Arrhenius dependence of the relaxation frequency coincides with the hopping-to-activated crossover found in direct current. This provides an operational criterion: the baseline is the reconstruction from the master curve, the measure of deviation is the frequency-median residual of $\log_{10}(\sigma'/\sigma_{dc})$ at each temperature, and the signature of a real change of response is a statistically significant monotonic relation of this residual with temperature (rank correlation at $p < 0.01$ over the number of temperatures, not the number of points). By this criterion the response of 0.5 M changes over the measured range, the change being both the largest in amplitude and the only one accompanied by an independent dc signature.

The approximate collapse of the spectra means that the shape of the frequency dispersion changes only weakly with temperature: what mainly changes is the characteristic frequency of the response, not its form. This leads to an important methodological remark. The exponent s in the Jonscher law [8] $\sigma'(\omega) = \sigma_{dc} + A \cdot \omega^s$, evaluated in a fixed frequency window, is widely used as a diagnostic of the hopping transport mechanism [9,11,35], yet even with an unchanged spectral shape it still varies with temperature, because the window falls on different parts of the master curve. The scale of the effect is shown by a direct test. The master curve is built by averaging all the reduced spectra of a sample; then for each temperature it is converted back into dimensional coordinates with that temperature's own $\sigma_{dc}(T)$ and $f_H(T)$, sampled on the real frequency grid and processed by the same procedure for determining s. The mechanism in such a reconstruction is unchanged by construction, and nevertheless 45–49 % of the observed swing of s(T) is reproduced. What follows is not that the remaining half of the swing is necessarily physical, but that s(T) taken without subtracting this contribution is not open to interpretation: only the residual $s(T) - s_{rec}(T)$ can be compared with mechanism models. This conclusion does not require superposition to hold exactly: it is obtained by reconstructing the spectra from one and the same unchanged master curve and does not depend on how accurately that curve describes the measured data. In what follows, therefore, temperature dependences are characterised by the position of the relaxation, which is determined directly and does not depend on the choice of window.

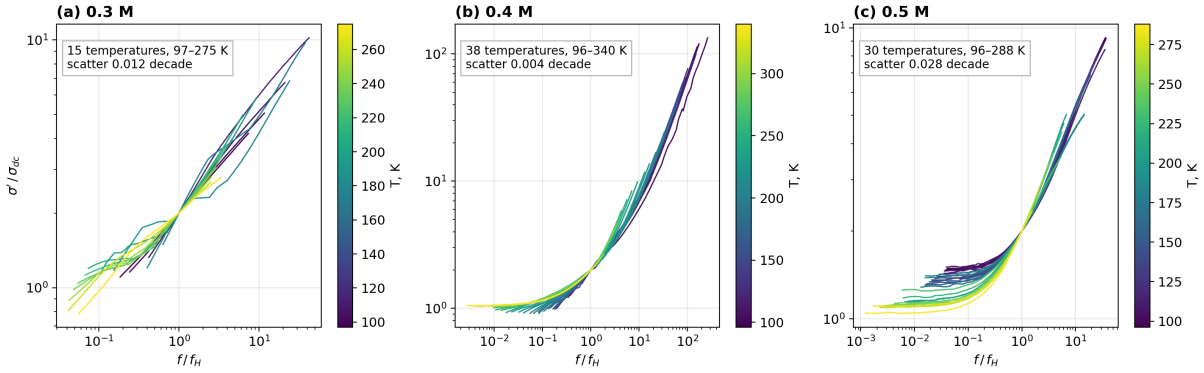


Fig. 10 Reduction of the conductivity spectra to a master curve: σ'/σ_{dc} versus f/f_H within the frequency window used (f below the crossover of the parasitic branch). Colour codes temperature; each panel states the number of temperatures, their interval and the median scatter of the curves

The temperature dependence of the relaxation frequency is shown in Fig. 11; the points obtained from the equivalent-circuit fit coincide with the independently located maxima of Z″(f). In every case the fit was performed only over points lying below the frequency at which the parasitic branch becomes significant (Section 2.2). For 0.5 M the dependence splits into two linear branches with a break near 200 K: 14.2 ± 0.6 meV over 97–201 K and 106 ± 5 meV over 210–370 K. The break falls inside the interval over which direct current shows the same crossover: for this sample the dc data depart from Mott linearity at 162 K and the local activation energy reaches its maximum only at 277 K (Section 3.3). The transition is extended in both measurements and neither locates it to better than a few tens of kelvin, but the two independent experiments

place it in the same range. For 0.3 M there are also two branches: 20.6 ± 0.4 meV over 97–131 K and 104 ± 17 meV over 200–260 K.

For the 0.4 M sample the slow relaxation gives 159 ± 6 meV over 195–340 K; its fast relaxation lies at 60–98 kHz, i.e. above the crossover frequency and in the region of the parasitic branch's own time constant (61 kHz), and is therefore excluded from consideration. This agrees with the dc activation energy (164 meV), with the estimate from the resistance of the same circuit element (157 ± 7 meV) and with the model-independent position of the Z'' maximum (177 ± 6 meV): four different routes agree to within 13 %, so the slow element corresponds to the same transport channel that is observed in direct current. The frequency of this relaxation shifts by a factor of 168 with temperature, and by a factor of 32 for 0.5 M, whereas the parasitic branch has a temperature-independent time constant; the observed relaxations therefore cannot be ascribed to it. A regularity common to all three samples is the monotonic decrease of the apparent activation energy with increasing frequency, from values close to those found in direct current at the low-frequency end down to a few meV at 100 kHz. The upper part of this range lies above the crossover frequencies of Section 2.2 and is quoted as a description of the raw data only; the trend itself is already established inside the analysed window. It is characteristic of hopping transport: the higher the frequency, the shorter and lower-barrier the hops that contribute to the response.

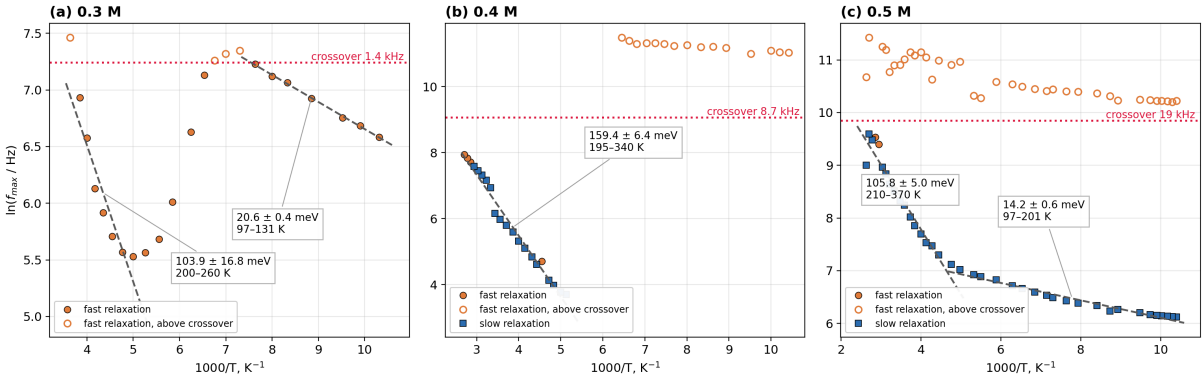


Fig. 11 Arrhenius plots of the dielectric relaxation frequency. Filled symbols are points below the crossover frequency of the parasitic branch (dashed line), over which the fit was performed; open symbols are points above it, excluded from the analysis

3.5. Comparison of the optical and transport characteristics

Bringing all the measurements together (Table 1) reveals a clear pattern. The transport characteristics vary monotonically: the parameter T_0, the dc activation energy and the conductivity improve successively from 0.3 M to 0.5 M.

The optical characteristics behave differently: the near-band-edge linewidth, the relative intensity of the defect emission and the doublet splitting ΔE_{12} are non-monotonic with an optimum at 0.4 M. Since the defect emission intensity is a direct optical measure of the point-defect content, its non-monotonicity means that the point-defect content and the disorder that governs charge transport are not the same characteristic: from 0.4 M to 0.5 M the defect emission grows by more than an order of magnitude while T_0 and the activation energy continue to fall. The morphology forms a third, independent characteristic: the grain size is the same throughout the series, while the large-scale inhomogeneity of the relief is greatest for 0.4 M – the sample that is best by the optical measures and intermediate by the transport ones. Surface relief, point-defect content and the disorder that controls charge transport thus vary as three independent characteristics.

A consistent link can be traced between the transport and optical characteristics: the doublet splitting ΔE_{12} is largest in the same samples in which the defect emission is stronger, which points to a defect-related origin of the low-energy component of the doublet – most probably recombination involving a shallow acceptor state.

No difference in the band-edge position between the samples is detected by any of the methods applied: extrapolation of the temperature dependence of the near-band-edge photoluminescence is sensitive to differences of about 10 meV and gives a spread of 6 meV, and the reflectance spectra, with systematics of order 90 meV, reveal no differences either. Meanwhile the conductivity changes by almost an order of magnitude and T_0 by more than an order. No band-structure differences could be found, and the observed transport differences are associated with states inside the band gap.

The links listed above are qualitative: they demonstrate a consistent variation of independently measured quantities but do not establish causal relations. Nevertheless, the consistency of the directions of change, obtained by independent techniques, makes the observed picture robust.

Table 1. Structural, optical and transport parameters of the ZnO films. The quantities are grouped by the character of their behaviour with precursor concentration: the monotonically varying dc charge-transport characteristics, the ac response characteristics, and the optical (structural) characteristics, most of which are non-monotonic with an optimum at 0.4 M.

Parameter	0.3 M	0.4 M	0.5 M
TRANSPORT CHARACTERISTICS – monotonic in concentration			
Parameter T_0, K	4.3×10^5	$(7.2 \pm 1.0) \times 10^4$	3.3×10^4
Activation energy (310–355 K), meV	233	164	95
R_s(300 K), Ω/sq	3.1×10^5	1.2×10^5	4.0×10^4
σ(300 K), S/cm	0.27	0.31	1.09
ALTERNATING CURRENT: response shape and relaxation			
Master-curve scatter, decades	0.012	0.004	0.028
Relaxation energy, low T, meV	20.6 ± 0.4 (97–131 K)	–	14.2 ± 0.6 (97–201 K)
Relaxation energy, high T, meV	104 ± 17 (200–260 K)	159 ± 6 (195–340 K)	106 ± 5 (210–370 K)
OPTICAL AND STRUCTURAL CHARACTERISTICS			
Band edge E_0 (PL, Varshni), eV	3.363	3.358	3.357
Near-band-edge linewidth (low T), meV	77.6	63.2	84.9
I_{def} / I_{NBE} at 300 K	3.15	< 0.037	0.49
Splitting ΔE_{12}, meV	42.6	21.5	26.8
Roughness S_q, nm	13.4	16.9	13.1
OTHER			
Quenching energy E_2, meV	not determined	264 ± 49	334 ± 30
Total NBE quenching (native range / up to 340 K)	1.7 / 2.6	4.8 / 4.2	8.0 / 4.5

4. Conclusions

The principal methodological result of this work is that the exponent of the Jonscher power law, evaluated in a fixed frequency window, cannot serve as an indicator of a change in the hopping transport mechanism. The conductivity spectra of all three samples collapse onto a single master curve with a scatter of 0.004–0.028 decades, and reconstructing the spectra from that unchanged curve reproduces 45–49 % of the observed temperature swing of the exponent. Temperature dependences are therefore characterised by the position of the dielectric relaxation, which is determined directly: for 0.4 M it gives 159 ± 6 meV against

164 meV in direct current, and for 0.5 M the break in the Arrhenius dependence, at ≈200 K, falls inside the extended interval over which direct current shows the crossover from hopping to activated transport.

The quality of the films is not described by a single parameter. The charge-transport characteristics improve monotonically: T_0 falls from 4.3×10^5 to 3.3×10^4 K, the activation energy from 233 to 95 meV, and the sheet resistance falls from 3.1×10^5 to 4.0×10^4 Ω/sq – the conductance rises by almost an order of magnitude. The optical characteristics behave non-monotonically: the near-band-edge linewidth and the relative intensity of the defect emission are optimal at 0.4 M, while the grain size is the same throughout the series and the large-scale inhomogeneity of the relief is greatest for 0.4 M. The point-defect content and the morphology are therefore not the parameters that control charge transport.

No difference in the band-edge position between the samples was found: photoluminescence gives a spread of 6 meV at a sensitivity of about 10 meV, and the reflectance spectra, at a substantially lower sensitivity, show no differences either – while the conductivity changes by almost an order of magnitude. The transport differences are thus determined by states inside the band gap rather than by the band structure. The splitting of the near-band-edge doublet follows the defect density, indicating a defect-related origin of its low-energy component.

From a practical standpoint the highest conductivity is provided by the 0.5 M concentration and the best optical quality by 0.4 M; the notion that the quality of ZnO films improves monotonically with increasing precursor concentration applies only to the charge-transport characteristics.

References

[1] Ü. Özgür, Ya.I. Alivov, C. Liu, A. Teke, M.A. Reshchikov, S. Doğan, V. Avrutin, S.-J. Cho, H. Morkoç, *J. Appl. Phys.* 98, 041301 (2005). https://doi.org/10.1063/1.1992666

[2] A. Janotti, C.G. Van de Walle, *Rep. Prog. Phys.* 72, 126501 (2009). https://doi.org/10.1088/0034-4885/72/12/126501

[3] J. Cho, S. Hwang, D.-H. Ko, S. Chung, *Materials* 12, 3423 (2019). https://doi.org/10.3390/ma12203423

[4] A. Arslanov, Sh. Yuldashev, N. Botirova, R. Nusretov, J. Murodov, J. Xudoyqulov, *Phys. Sci. Int. J.* 29, 29–35 (2025). https://doi.org/10.9734/psij/2025/v29i1871

[5] M. Lamri Zeggar, N.E.H. Touidjen, M.S. Aida, N. Aouabdia, S. Rouabah, *J. Opt.* 52, 1782–1788 (2023). https://doi.org/10.1007/s12596-022-01079-5

[6] T.V.K. Karthik, A.G. Hernández, Yu. Kudriavtsev, H. Gómez-Pozos, M.G. Ramírez-Cruz, L. Martínez-Ayala, A. Escobosa-Echvarria, *J. Mater. Sci.: Mater. Electron.* 31, 7470–7480 (2020). https://doi.org/10.1007/s10854-020-02987-7

[7] C.M. Mahajan, M.G. Takwale, *Micro Nanostruct.* 163, 107131 (2022). https://doi.org/10.1016/j.spmi.2021.107131

[8] A.K. Jonscher, *Nature* 267, 673–679 (1977). https://doi.org/10.1038/267673a0

[9] M. Salah, S. Azizi, A. Boukhachem, C. Khaldi, M. Amlouk, J. Lamloumi, *Appl. Phys. A* 125, 616 (2019). https://doi.org/10.1007/s00339-019-2911-3

[10] F. Ahmad, A. Maqsood, *Mater. Sci. Eng., B* 273, 115431 (2021). https://doi.org/10.1016/j.mseb.2021.115431

[11] F. Ahmad, A. Maqsood, *Physica E* 143, 115353 (2022). https://doi.org/10.1016/j.physe.2022.115353

[12] S. Karakaya, *J. Nanoelectron. Optoelectron.* 13, 677–686 (2018). https://doi.org/10.1166/jno.2018.2196

[13] F.Z. Acar, R. Ertuğrul Uyar, A. Tataroğlu, *Silicon* 18, 25–33 (2025). https://doi.org/10.1007/s12633-025-03545-8

[14] Y.P. Varshni, *Physica* 34, 149–154 (1967). https://doi.org/10.1016/0031-8914(67)90062-6

[15] J.R. Ramos-Serrano, S. Alcántara-Iniesta, M. Acosta-Osorno, M.E. Calixto, *Mater. Sci. Semicond. Process.* 144, 106585 (2022). https://doi.org/10.1016/j.mssp.2022.106585

[16] A.L. Patterson, *Phys. Rev.* 56, 978–982 (1939). https://doi.org/10.1103/PhysRev.56.978

[17] K. Vanheusden, W.L. Warren, C.H. Seager, D.R. Tallant, J.A. Voigt, B.E. Gnade, *J. Appl. Phys.* 79, 7983–7990 (1996). https://doi.org/10.1063/1.362349

[18] A. Mandal, A.G. Banpurkar, S.D. Shinde, S.M. Jejurikar, *J. Appl. Phys.* 136, 025302 (2024). https://doi.org/10.1063/5.0205885

[19] K.P. O'Donnell, X. Chen, *Appl. Phys. Lett.* 58, 2924–2926 (1991). https://doi.org/10.1063/1.104723

[20] J. Tauc, R. Grigorovici, A. Vancu, *Phys. Status Solidi B* 15, 627–637 (1966). https://doi.org/10.1002/pssb.19660150224

[21] X. Meng, Y. Zhou, X. Zeng, X. Chen, Y. Chu, *J. Lumin.* 195, 201–208 (2018). https://doi.org/10.1016/j.jlumin.2017.11.036

[22] H. Shibata, *Jpn. J. Appl. Phys.* 37, 550 (1998). https://doi.org/10.1143/JJAP.37.550

[23] V.Sh. Yalishev, Sh.U. Yuldashev, Kh.T. Igamberdiev, T.W. Kang, B.H. Park, *J. Korean Phys. Soc.* 64, 1–5 (2014). https://doi.org/10.3938/jkps.64.1

[24] N.F. Mott, *J. Non-Cryst. Solids* 1, 1–17 (1968). https://doi.org/10.1016/0022-3093(68)90002-1

[25] B.T. Benton, B.L. Greenberg, E. Aydil, U.R. Kortshagen, S.A. Campbell, *Nanotechnology* 29, 415202 (2018). https://doi.org/10.1088/1361-6528/aad6ce

[26] S. Pal, T.K. Dalui, D. Basak, *J. Alloys Compd.* 946, 169335 (2023). https://doi.org/10.1016/j.jallcom.2023.169335

[27] A.G. Zabrodskii, *Philos. Mag. B* 81, 1131–1151 (2001). https://doi.org/10.1080/13642810108205796

[28] A.L. Efros, B.I. Shklovskii, *J. Phys. C: Solid State Phys.* 8, L49–L51 (1975). https://doi.org/10.1088/0022-3719/8/4/003

[29] Y. Zhang, *Microelectron. Int.* 43, 13–18 (2025). https://doi.org/10.1108/MI-05-2025-0078

[30] D. Tolera, T. Senbeta, B. Mesfin, *Sci. Rep.* 15, 30342 (2025). https://doi.org/10.1038/s41598-025-13210-0

[31] R. Ghosh, R. Majumder, S. Kundu, M. Pradhan, S. Roy, R. Gayen, M. Pal Chowdhury, *J. Mater. Sci.* 56, 19128–19143 (2021). https://doi.org/10.1007/s10853-021-06459-z

[32] A. Ghosh, A. Pan, *Phys. Rev. Lett.* 84, 2188–2190 (2000). https://doi.org/10.1103/PhysRevLett.84.2188

[33] D.L. Sidebottom, *Phys. Rev. Lett.* 82, 3653–3656 (1999). https://doi.org/10.1103/PhysRevLett.82.3653

[34] I. Elhamdi, F. Mselmi, H. Souissi, S. Kammoun, E. Dhahri, P. Sanguino, B.F.O. Costa, *RSC Adv.* 13, 3377–3393 (2023). https://doi.org/10.1039/D2RA07701A

[35] S.R. Elliott, *Adv. Phys.* 36, 135–217 (1987). https://doi.org/10.1080/00018738700101971

Statements and Declarations

Funding: This work was supported by the Ministry of Higher Education, Science and Innovation of the Republic of Uzbekistan (Grant No. FZ-2020092435).

Competing Interests: The authors have no relevant financial or non-financial interests to disclose.

Author Contributions: A.A. Nebesniy: Investigation, Methodology, Software, Formal analysis, Data curation, Visualization, Writing – original draft. A.O. Arslanov: Investigation, Methodology, Formal analysis, Data curation, Writing – original draft. P.B. Parchinskiy: Writing – review and editing. A.A. Nasirov: Resources, Writing – review and editing. Sh.U. Yuldashev: Conceptualization, Supervision, Writing – review and editing.

Data Availability: The data that support the findings of this study are available within the article and are available from the corresponding author upon reasonable request.